Flow response to large-scale topography: the Greenland tip jet

By JAMES D. DOYLE[1]* and MELVYN A. SHAPIRO[2], [1]*Naval Research Laboratory, Monterey, CA;* [2]*NOAA Environmental Technology Lab. and National Center for Atmos. Research, Boulder, CO, USA*

ABSTRACT

Numerical model simulations of idealized and observed flows are used to investigate the dynamics of low-level jet streams that form in stratified flow downstream of the vertex of large elliptical barriers such as the southern tip of Greenland, hereafter referred to as "tip jets". The tip jet dynamics are governed by conservation of Bernouli function as parcels accelerate down the pressure gradient during orographic descent. In some circumstances, the Greenland tip jet is influenced by baroclinic effects such as differential horizontal (cross-stream) thermal advection and/or vertical shear. In contrast, in the barotropic situation upstream flow is diverted around and over the obstacle into laminar (Bernouli conservation) and turbulent (Bernouli deficit) regimes, respectively. In both situations, a downstream geostrophic balance is achieved, characterized by baroclinicity and vertical shear associated with the surface-based tip-jet front. The strength of the tip-jet is most sensitive to changes in the basic state dimensionless mountain height (Nh/U) and Rossby number, underscoring the importance of the orographic deflection of airstreams and Lagrangian accelerations on the slope. Enhanced surface-based forcing of the ocean circulation occurs in the region of the tip jet core through large air–sea energy exchange (upward surface-heat fluxes >800 W m^{-2}), and at the tip jet flank through localized surface stress forcing.

1. Introduction

The orographic modification of stably-stratified air flow past a topographic obstacle has been the focus of numerous investigations. In some situations, orographic flows may be strongly influenced by the earth's rotation, such as for a large-scale obstacle (Eliassen, 1980; Thorsteinsson, 1988) or in the presence of low-level blocking or cold-air damming (Pierrehumbert and Wyman, 1985; Thorsteinsson and Sigurdsson, 1996; Schutts, 1998). Although there has been considerable research in many aspects of idealized low-level

three-dimensional flow in the vicinity of isolated topography (Snyder et al., 1985; Smolarkiewicz and Rotunno, 1989) and associated downstream wake dynamics (Schär and Smith, 1993; Smith et al., 1997), questions remain regarding the nature of flow responses to realistic obstacles such as Greenland, the Alps, the Antarctic Peninsula (Buzzi et al., 1997), and the Tibetan Plateau, and in particular, the structure and dynamics of topographically-induced downstream low-level jets.

The three-dimensional flow past large-scale topography, such as Greenland, can be particularly complex because of multi-scale orographic features and associated boundary-layer processes. The topography of Greenland (Fig. 1) is characterized by extremely steep terrain near the coastlines, an ice-covered plateau exceeding 3000 m, and a continuous spectrum of mountain widths ranging

---

* Corresponding author: James D. Doyle, Naval Research Laboratory, Marine Meteorology Division, 7 Grace Hopper Avenue, Monterey, CA 93943-5502, USA. E-mail: doyle@nrlmry.navy.mil.

1. REPORT DATE **07 MAY 1999**	2. REPORT TYPE	3. DATES COVERED **00-00-1999 to 00-00-1999**

4. TITLE AND SUBTITLE **Flow response to large-scale topography: the Greenland tip jet**	5a. CONTRACT NUMBER
	5b. GRANT NUMBER
	5c. PROGRAM ELEMENT NUMBER
6. AUTHOR(S)	5d. PROJECT NUMBER
	5e. TASK NUMBER
	5f. WORK UNIT NUMBER

7. PERFORMING ORGANIZATION NAME(S) AND ADDRESS(ES) **Naval Research Laboratory,7 Grace Hopper Ave., Stop 2 ,Monterey,CA,93943-5502**	8. PERFORMING ORGANIZATION REPORT NUMBER
9. SPONSORING/MONITORING AGENCY NAME(S) AND ADDRESS(ES)	10. SPONSOR/MONITOR'S ACRONYM(S)
	11. SPONSOR/MONITOR'S REPORT NUMBER(S)

12. DISTRIBUTION/AVAILABILITY STATEMENT **Approved for public release; distribution unlimited**

13. SUPPLEMENTARY NOTES

14. ABSTRACT **see report**

15. SUBJECT TERMS

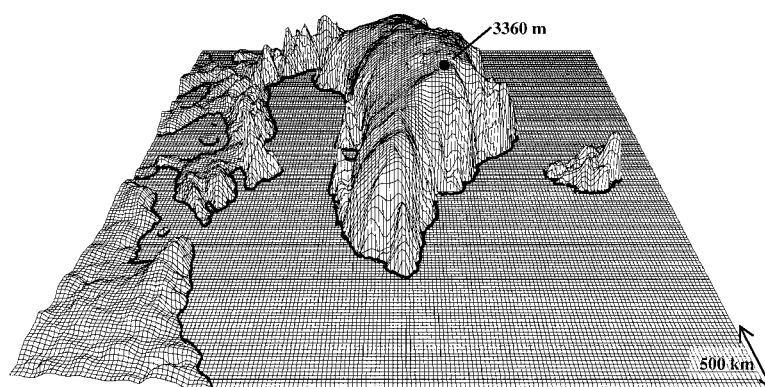| 16. SECURITY CLASSIFICATION OF:			17. LIMITATION OF ABSTRACT **Same as Report (SAR)**	18. NUMBER OF PAGES **21**	19a. NAME OF RESPONSIBLE PERSON
a. REPORT **unclassified**	b. ABSTRACT **unclassified**	c. THIS PAGE **unclassified**			

Fig. 1. Three-dimensional depiction of the Greenland relief.

from cross-mountain half widths of less than 150 km in the south to greater than 500 km in the central portion. The study of flow modification by Greenland, specifically at the southern vertex or Cape Farewell (Uummannarsuaq) (Fig. 2), is a challenge for a variety of reasons that include its extreme topography, the proximity to the semi-permanent Icelandic cyclone, and high-latitude air–sea interaction processes. Danish weather forecasters have been aware for some time of frequent high wind events downstream of Cape Farewell in low-level west/northwest flow conditions (personal communication, Leif Rasmussen, Senior Forecaster Danish Meteorological Institute, 1999). These lower-boundary jets are clearly linked to the large-scale topography of Greenland and represent a significant hazard to commercial shipping industries, military operations, and scientific field studies in this area.

The purpose of this investigation is to explore the dynamical aspects of flow past large-scale elliptical topographic obstacles with special emphasis on the formation of lower-boundary jet streams emanating from the vertex of the orographic ellipsoid or "tip". This study presents numerical simulations of idealized and observed flows impinging upon topography representative of Greenland. An overview of the established relevant theoretical studies is discussed in Section 2, followed by a description of the model architecture in Section 3. The results from a series of numerical experiments performed with idealized flows are presented in Section 4. Section 5 presents two numerical simulations of observed flows in the vicinity of Greenland that occurred during the

Fronts and Atlantic Storm-Track EXperiment (FASTEX) (Joly et al., 1997). The discussion of the results and suggestions for future research follow in Section 6.

2. Theoretical overview

The dynamical parameter space governing the occurrence of flow stagnation and flow splitting upstream of isolated three-dimensional topography in the absence of rotation has been investigated by numerous authors (Smith, 1980, 1989, Smolarkiewicz and Rotunno, 1989). Through scale analysis, the governing parameters for orographic flow in the non-rotating frame of reference have been identified as the aspect ratio, obstacle shape, and the dimensionless obstacle height (or inverse Froude number), $\hat{h} = N h_m / U$, where N is the Brunt–Väisälä frequency, h_m is the mountain height, and U is the upstream wind (Smith, 1989; Smith and Grønás, 1993). These studies suggest that the dimensionless obstacle height acts as the control parameter, which determines the transition point from flow over the topography to flow around (splitting) the obstacle. In the case of a two-dimensional ridge, the critical value for flow stagnation is $\hat{h}_c \sim 0.85$ (Huppert and Miles, 1969), while for a symmetric Gaussian obstacle the critical value is larger, $\hat{h}_c \sim 1.1$ (Smith and Grønás, 1993). Stratified flow past an obstacle when $\hat{h} \ll 1$ is generally explained by linear theories (Smith, 1980), while for $\hat{h} > 1$ the nonlinear regime prevails (Smolarkiewicz and Rotunno, 1989, Smith, 1989).
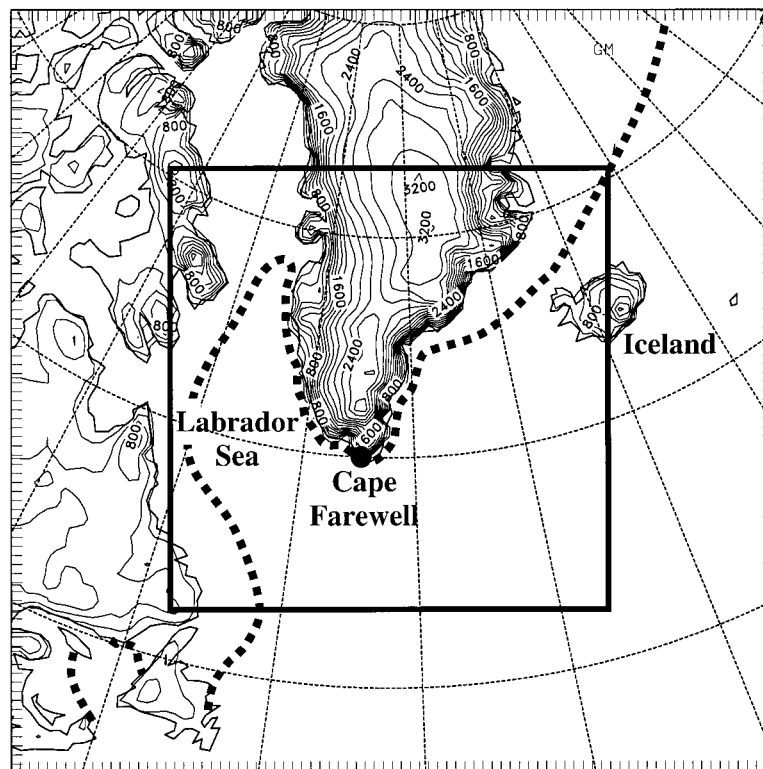
Fig. 2. The outer-grid mesh ($\Delta x = 45$ km) topography and inner-grid mesh ($\Delta x = 15$ km) location for the numerical simulations of observed flows. The contour interval is 200 m. The mean ice edge during early February 1997, as determined by SSM/I observations of observed flows, is shown by the dashed line.

Thus, the dimensionless obstacle height represents a measure of the nonlinearity of the flow.

The orographic-flow dynamics for the rotating case are governed by $\hat{h}$, as well as the mountain Rossby number, $R_o = U/fL$, where f is the Coriolis parameter and L is the mountain half width (Gill, 1982; Pierrehumbert and Wyman, 1985; Thorsteinsson, 1988). For $R_o > 10$, weak rotational influences occur and the response is primarily governed by vertically propagating gravity waves (Gill, 1982). For the case $R_o \sim 1$, inertia-gravity waves dominate, which are characterized by quasi-horizontal energy propagation and relatively small vertical wavelength (Pierrehumbert, 1984; Trüb and Davies, 1995). In this intermediate R_o regime, with L greater than ~ 50 km, the inertial effects may be significant (Smith, 1979). Trüb and Davies (1995) found that for flow over broad terrain ($R_o < 1$) a buoyancy wave response results from the forcing of ageostrophic flow by

the balanced flow. In the case of strong rotational influence ($R_o \ll 1$), the flow over synoptic-scale orography ($L > 1000$ km) results in evanescent quasi-geostrophic waves (Gill, 1982) and the elimination of mountain waves (Queney, 1948). Smith (1979) notes that quasi-geostrophic flow over large-scale orography leads to leftward-deflected streamlines as the flow approaches the topography, due to vertical stretching, and decreased parcel velocity and Coriolis force. At the mountain top, the air flow re-accelerates concurrent with the increased vertical potential temperature gradient and the streamlines curve back to the right, with no permanent deflection in the downstream. For large-scale mountains, the variation of Coriolis force with latitude, or the so-called "beta effect", can impart a net cyclonic vorticity to the downstream flow leading to troughing in the lee (Hess and Wagner, 1948).

The tendency for lee-cyclone development to

occur results, in part, as consequence of flow impinging on synoptic-scale and mesoscale topography (see review by Tibaldi et al. (1990)). The semi-permanent Icelandic cyclone highlights the role of the extreme topography of Greenland in the active lee-cyclone processes of this region (Scorer, 1988). Numerous theories of lee cyclogenesis have been advanced that attempt to account for the modification of baroclinic instability in the presence of an orographic barrier. Smith (1986) proposed a linear theory that describes a stationary wave that may be excited due to a resonant response to the topography. Davis (1997) performed diagnostics and analysis of quasi-geostrophic model results and found the topographically modified surface potential temperature distribution was of primary importance in the modification of baroclinic waves in the presence of mountains. The theory of Pierrehumbert (1985) reproduces many of the characteristics of lee cyclogenesis through the application of a simple model that describes baroclinic instability modulation due to low-level blocking by a barrier.

The upstream influence associated with low-level blocking is initiated in two dimensions near $\hat{h} \sim 0.75$ (Pierrehumbert and Wyman, 1985). The blocking forces local deceleration, which results in upstream subgeostrophic flow and predominantly leftward deflection around the obstacle (Smith, 1982). Pierrehumbert and Wyman (1985) concluded, based on two-dimensional numerical model results, that the Coriolis force inhibits the upstream influence of blocking through geostrophic adjustment. The results of Pierrehumbert and Wyman suggest that the length scale of the upstream influence for blocked flow is governed by the Rossby radius of deformation, $L_d = N h_m / f$. Thorsteinsson (1988) applied a three-dimensional isentropic model to flow over and around a symmetric 3-D obstacle on an f-plane and found the magnitude of the wind speed minima and maxima to be most sensitive to $\hat{h}$ and the location to R_o. For elongated topography, the lateral airstream deflection is most sensitive to the mountain aspect ratio, $\alpha = L_x / L_y$, where L_x is the along-stream width and L_y is the width in the cross-stream direction (Thorsteinsson and Sigurdsson, 1996). Rotational effects can modulate the pressure drag (Ólafsson and Bougeault, 1997), and downstream

conditions through distortion and erosion of lee-side vortices and wakes (Peng et al., 1995).

3. Numerical model architecture

The numerical simulations of idealized and observed flows for this study were prepared with the atmospheric portion of the Naval Research Laboratory's Coupled Ocean-Atmosphere Mesoscale Prediction System (COAMPS) (Hodur, 1997). The model is a finite-difference approximation to the fully compressible, nonhydrostatic equations that govern atmospheric motions. The equations are solved in three dimensions with a terrain-following vertical coordinate, σ_z (Gal-Chen and Somerville, 1975). The finite difference schemes are of second-order accuracy in time and space. A time splitting technique that features a semi-implicit treatment for the vertical acoustic modes enables efficient integration of the compressible equations (Klemp and Wilhelmson, 1978; Durran and Klemp, 1983). Reflection of waves at the upper boundary is suppressed by a gravity wave absorbing layer using a Rayleigh damping technique in the upper 13 km of the model domain based on the work of Durran and Klemp (1983).

Both idealized and real-data model simulations make use of a prognostic equation for the turbulent kinetic energy (TKE) budget to represent the planetary boundary-layer and free-atmospheric turbulent mixing and diffusion. The surface fluxes are computed following the Louis (1979) formulation, which makes use of a surface energy budget based on the force-restore method. The subgrid-scale moist convective processes are parameterized using an approach following Kain and Fritsch (1993). The explicit grid-scale evolution of the moist processes are explicitly predicted from budget equations for cloud water, cloud ice, rain drops, snow flakes, and water vapor (Rutledge and Hobbs, 1983). The short- and long-wave radiation processes are parameterized following Harshvardhan et al. (1987). The simulations of observed flows use the full suite of physical parameterizations. For simplicity, the idealized simulations are adiabatic and inviscid, with the free-atmosphere vertical diffusion derived from the explicitly predicted TKE.

A series of simplified idealized numerical simulations based upon synthetic initial conditions were

performed to isolate the relevant dynamics of flow impinging upon large-scale topographic barriers. The domain configuration for these idealized initial condition numerical experiments used a single grid with 175×175 point and a horizontal grid increment of 35 km. The model top is at 20 km with 40 irregularly spaced vertical levels. A Gaussian-shaped mountain,

$$h = h_m \exp \left[- \left(\frac{x}{L_x} \right)^2 - \left(\frac{y}{L_y} \right)^2 \right], \qquad (1)$$

where h_m, is the maximum mountain height, and L_x and L_y represent the mountain half-width in the x and y directions, is used to represent the topography. The lateral boundary condition formulation is based on a radiative condition (Orlanski, 1976) with a prescribed group velocity that is invariant in time. Numerical experimentation revealed little sensitivity to the steady-state solution for reasonable prescribed group velocities. In these idealized simulations, a digital filter (Lynch and Huang, 1992) is used for initialization in order to minimize spurious modes forced by the impulsive start. The idealized simulations are performed on an f-plane for a latitude of $65°N$ ($f = 1.3 \times 10^{-4}$).

The domain configuration for the simulations of observed flows contains two horizontally nested grid meshes of 85×85 and 145×145 points, respectively (Fig. 2). The horizontal grid increment of the computational meshes are 45 km and 15 km, respectively. The model top is at 31 km with 40 irregularly spaced vertical levels. An incremental update data assimilation procedure that enables mesoscale phenomena to be retained in the analysis increment fields is used to initialize these simulations. The initial fields for the model are created from multivariate optimum interpolation analyses of upper-air sounding, surface, aircraft and satellite data that are quality controlled and blended with the 12-h COAMPS forecast fields. Real-data lateral boundary conditions make use of Navy Operational Global Analysis and Prediction System (NOGAPS, Hogan and Rosmond, 1991) forecast fields following Davies (1976). The topographic data for the simulations are based on the U.S. Defense Mapping Agency's 100-m resolution data set. The model terrain field for the first mesh (Fig. 2) shows that the

steep topography of Greenland is adequately represented.

4. Numerical simulations of flows past idealized topography

A series of numerical experiments were undertaken to identify the dynamical sensitivity of flow past an elliptically-shaped Gaussian obstacle analogous to Greenland. The initial discussion focuses on two idealized simulation: with and without the earth's rotation (f-plane). The topographic obstacle in the flow is described by eq. (1) with a maximum height of 3000 m. Nondimensional scaling parameters for these two simulation are $\hat{h} = 3.0$, $R_o = 0.38$ and $\alpha = 4.0$. The simulations were integrated to 144 h, with a quasi-steady state flow field achieved after 96 h or a nondimensional time of $Ut/L \sim 17$. The 10-m winds for the two simulations are shown in Fig. 3. The 10-m winds for the simulation with rotation (Fig. 3a) indicate preferential flow to the left on the upstream side of the obstacle in agreement with the established theory (Smith, 1982; Pierrehumbert and Wyman, 1985) and simulations (Peng et al., 1995; Thorsteinsson and Sigurdursson, 1996). The largest acceleration occurs within the upstream flow over the northern half of the obstacle, where the Coriolis force acts to rotate the balanced barrier jet flow towards the mountain. Here the kinetic energy is sufficiently large to ascend the barrier and pass over the ridge, and decelerate in the lee. The largest acceleration over the southern portion of the mountain is down the pressure gradient in the lee, with continued rightward deflection due to the Coriolis force. A wind speed minimum and lee-eddies are apparent in the downstream wake. A series of wind maxima resulting from inertia-gravity wave generation exists in the northern portion of the wake. The southern portion of the wake (Fig. 3a) is flanked by a narrow low-level jet stream as the flow separates from the obstacle tip, hereafter referred to as the "tip jet", which is the primary focus of the present discussion. Smith et al. (1997) referred to a similar lower-boundary wind flow response as a "corner wind". The accelerated flow to the south of the wake reaches a maximum approximately $3L$ downstream from the ridge line. In the downstream, the tip jet approaches geostrophic balance with the low-level pressure field.
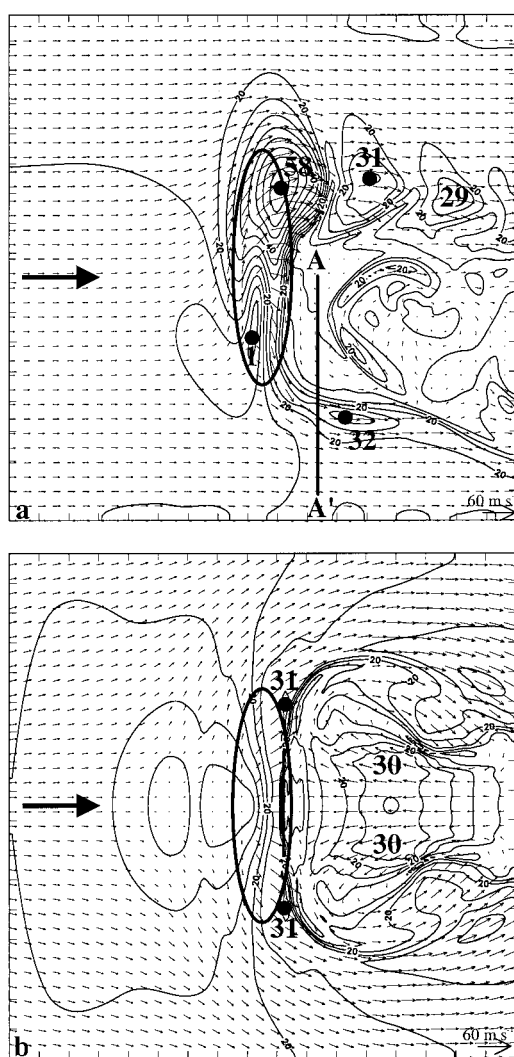
Fig. 3. The lowest model-level (10 m) wind speed and vectors (every 5 grid points) for simulations (a) on an *f*-plane and (b) without rotation (96 h). The isotach interval is 2.5 m s^{-1}. The tick mark spacing on the boundary represents a distance of 300 km (10 grid intervals). The 750-m terrain contour ($h/4$) is shown by the bold ellipse.

Geostrophic adjustment occurs relatively rapidly at the latitude of Greenland (65°N) with a quasi-balanced gradient flow obtained $\sim L_d$ (350 km) downstream of the lee. Analysis of the simulated momentum budget in the vicinity of the tip-jet maximum (not shown) confirms this transition to a balance dominated by the cross-flow pressure gradient and Coriolis force.
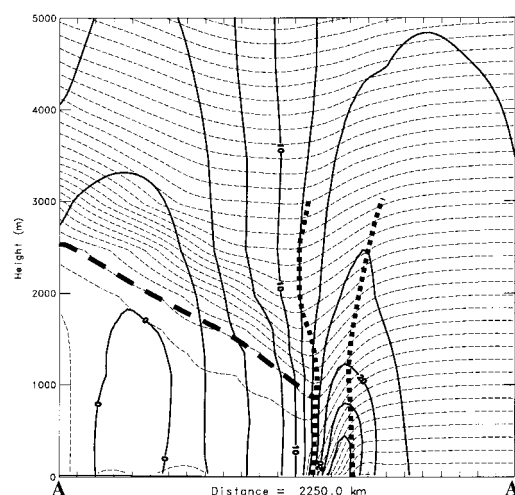
Fig. 4. Vertical cross section of potential temperature (dashed) and section-normal wind speed (solid) for the simulation on an *f*-plane taken along line AA′ of Fig. 3a. The isotherm interval is 1 K and the isotach interval is 2.5 m s^{-1}. Short-dashed lines designate the tip-jet frontal zone. The long-dashed line represents the inversion base capping the top of the well-mixed wake. The tick mark spacing on the abscissa represents a distance of 300 km (10 grid intervals).

Fig. 4 presents the vertical cross section potential temperature and section normal velocity component along the cross-section projection line AA′ of Fig. 3a, positioned in the lee of obstacle and transecting the low-level jet. The baroclinicity (with warm air to the north) associated with the surface-based tip jet appears as a frontal zone, or "tip-jet front", in first-order geostrophic thermal balance with the negative front-parallel shear above the jet. For example, the vertical shear in the lowest kilometer of the tip-jet front (5 m s^{-1} km^{-1}) is in approximate geostrophic thermal wind balance with the cross-jet thermal gradient (8 K (600 km)$^{-1}$) with little flow directed across the pressure gradient. The lateral shear and stratification associated with the topographic tip jet and front are consistent with a surface-based potential vorticity (PV) filament, as shown in Fig. 5. The generation of the surface-based PV filament appears to be consistent with the dissipative region upstream associated with low-level wave breaking. The asymmetrical velocity response with lee-cyclone transients in the wake (Fig. 3a) is contrasted with the symmetrical large-scale vortex
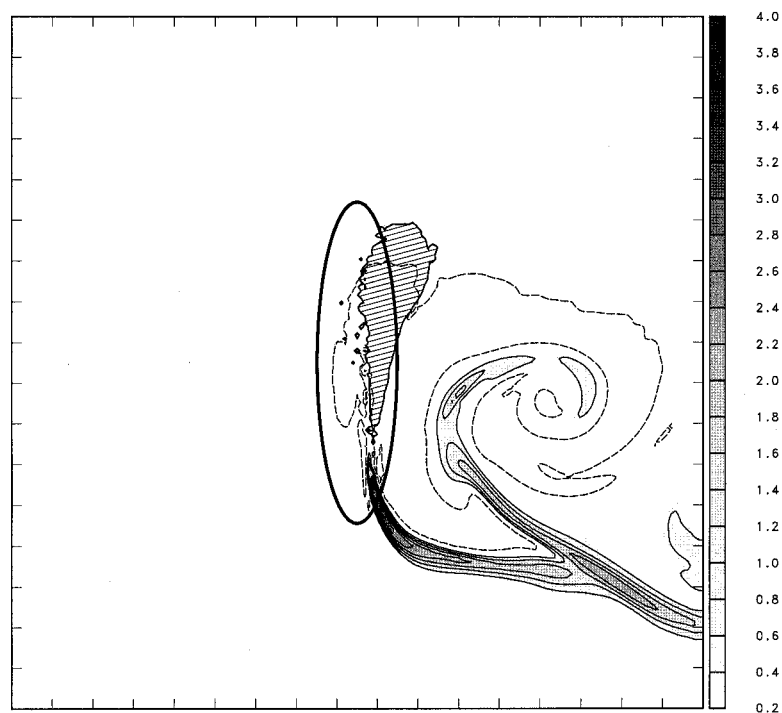
Fig. 5. Perturbation potential vorticity field at the 10-m level. The contour interval is 0.5 pvu (1 pvu = 10^{-6} K m^2 s^{-1} kg^{-1}). The region where the turbulent dissipation is active is represented by the hatching. The tick mark spacing on the boundary represents a distance of 300 km (10 grid intervals). The 750-m terrain contour ($h/4$) is shown by the bold ellipse.

shedding for the simulation without rotation ($f = 0$) (Fig. 3b). This result is in agreement with various other numerical simulations of flow past elliptical obstacles (Peng et al., 1995; Ólafsson and Bougeault, 1996). Smith (1982) addressed the theory of flow impinging on a finite north–south mountain range ($\alpha = 3.0$), which included the Coriolis force. His results indicate a northward deflection of the main upstream flow with an enhanced pressure gradient in the lee of the southern obstacle tip. The pressure distribution for the present experiments (not shown) is consistent with those presented by Smith (1982, Fig 11). Additionally, the vertical displacement response near the end of the obstacle is in qualitative agreement with the linear theory for flow around ridges established by Smith (1980).

Fig. 6 illustrates the along-obstacle variations in wave breaking inferred by the turbulent kinetic energy (TKE). Since, shear and buoyancy effects present in non-breaking flow may result in TKE production, which suggests some caution should be exercised when correlating TKE maxima with wave breaking. Nevertheless, TKE and potential temperature in vertical cross section are used here to highlight regions of turbulent mixing that likely are associated with wave breaking. The TKE is a maximum along the 271 K surface over the northern portion of the obstacle in the lee, as shown in the AA' section (upper left in Fig. 6). Along the southern portion of the obstacle (BB' section, lower left in Fig. 6), the mountain wave amplitudes are less pronounced with no wave breaking, in agreement with the results of Ólafsson and Bougeault (1997). This asymmetry in the breaking pattern arises from the influence of rotation, which leads to a stronger cross-mountain component along the northern portion of the obstacle due to the upstream flow diversion. A consequence of the differential wave breaking appears to be enhanced downslope warming associated with turbulent vertical mixing in the wake.
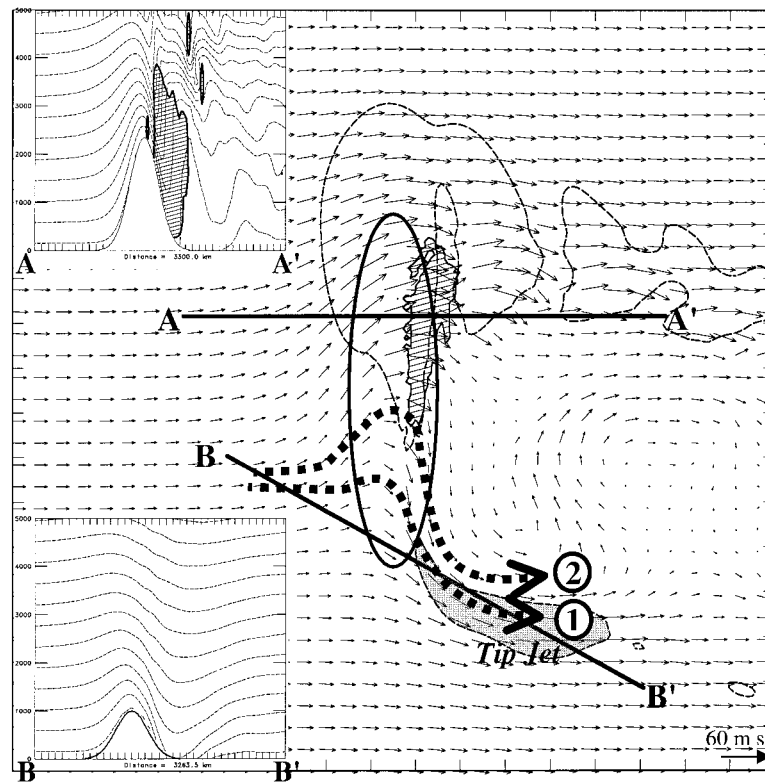
Fig. 6. The wind vectors (every 5 grid points) and 20 m s^{-1} isotach (tip-jet shaded) on the 271 K isentropic surface. Vertical cross sections of potential temperature (3 K isotherm interval) are shown for along line AA′ (upper left) and line BB′ (lower left). Schematic streamlines 1 and 2 are shown by the dotted lines. The region where the turbulent kinetic energy exceeds 1 m^{-2} s^{-2} is represented by the hatching in the horizontal and vertical sections. The tick mark spacing on the boundary represents a distance of 300 km (10 grid intervals). The 750-m terrain contour ($h/4$) is shown by the bold ellipse.

The tip-jet response to flow over/around topography can be interpreted in terms of Bernouli function, B,

$$B = C_p T + \frac{v^2}{2} + gz, \qquad (2)$$

where T is the temperature, v is the wind speed, and z is the height (see e.g., Schär, 1993; Schär and Durran, 1997, Pan and Smith, 1999). A nonzero potential vorticity flux is manifested as a gradient in B along an isentropic surface (Schär, 1993). Within the uncertainties that numerical model approximations introduce, air parcels that comprise the tip jet conserve B because of minimal dissipative processes, such as wave breaking, along their trajectories. For example, the 271 K isentropic surface descends by more than 1000 m from

the quiescent upstream to the vicinity of the tip jet in the lee, while the temperature increases slightly, and the velocity nearly doubles. Thus, the tip jet can be interpreted as a balanced Bernouli response to flow that is forced to pass over the mountain, descending down the lee slope at the vertex of the elliptical obstacle. Consider two adjacent streamlines shown in Fig. 6, where: (i) streamline 1 passes over the obstacle and then descends into the tip jet core (~ 23 m s^{-1}), and (ii) streamline 2 ascends the obstacle, passes through the wave breaking region and descends into the speed deficit in the wake (less than 10 m s^{-1}). It is clear that the air parcels flowing along streamline 1 escape Bernouli loss, while accelerating down the pressure gradient into the tip jet. In contrast, air parcels along streamline 2

experience a Bernouli deficit as they pass through the region of dissipative wave breaking. The tip-jet response to differences in Bernouli balance along adjacent parcel trajectories is similar to that discussed by Pan and Smith (1999) for gap flows.

To define the dynamical parameter space governing the tip jet response, a series of simulations were performed with various combinations of $\hat{h}$ (Nh/U), R_o and α for flow on an f-plane. The results are summarized in Fig. 7 and expressed as a function of u_{max}/U, which represents the nondimensional tip-jet speed (ratio of the 10-m tip jet maximum to the basic state wind speed). As $\hat{h}$ is increased for a specified R_o (Fig. 7a), the tip jet speeds increase in magnitude in response to the increased low-level flow acceleration down the pressure gradient along the obstacle lee slope. This result is not particularly sensitive to moderate changes in R_o. For small R_o, the flow is within the quasi-geostrophic regime where parcel acceleration is small compared to the Coriolis force resulting in a weaker tip-jet response (Fig. 7b). For large R_o, the inertial acceleration is of comparable magnitude to the Coriolis force consistent with large accelerations as parcels descend the lee into the tip jet. The tip jet response is moderately sensitive to the obstacle aspect ratio, α (Fig. 7c), particularly for larger $\hat{h}$, illustrating the importance of flow diversion and tip jet acceleration for elongated obstacles. In general, as the barrier is elongated in the cross-stream direction, the tip jet increases in intensity for the larger $\hat{h}$ regime (e.g., $\hat{h} = 4.4$).

5. Simulations of observed tip jets

The above-described simulations of flow past elliptical topography serve as a theoretical hypothesis for the investigation of similar flows in nature. Two such examples of tip jets in the lee of Greenland served as a motivation for the further COAMPS simulations discussed in this section. The model architecture used was previously detailed in Section 3. The first example was noted initially (but not investigated) in the simulation of a breaking gravity wave event observed over Greenland with the NOAA G-4 research aircraft on 29 January 1997 (Doyle et al., 1998) (FASTEX IOP 8). The second example occurred to the
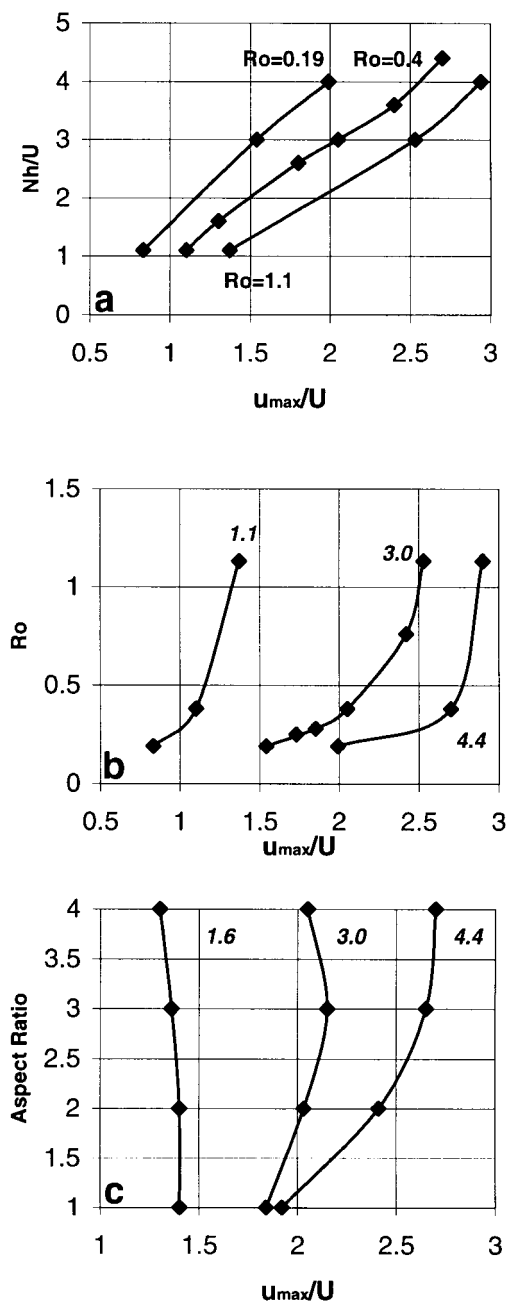

Fig. 7. The dependence of the nondimensional tip jet speed (u_{max}/U) as a function of (a) (Nh/U) with R_o specified, (b) R_o with $\hat{h}$ specified, and (c) aspect ratio with $\hat{h}$ specified.

northwest of a synoptic-scale cyclone development during 17–18 February 1997 (FASTEX IOP 17).

5.1. The 29 January 1997 Greenland tip jet

Fig. 8 presents the 18-h simulation of the Greenland tip-jet event valid at 0600 UTC 29 January 1997. Figure 8a presents the 600-hPa geopotential height and wind velocity field, which shows 30 m s^{-1} westerly flow over the southern portion of Greenland, situated between an upstream ridge and downstream trough. In the upstream, weaker (15 m s^{-1}) westerly flow is present. A distinct signature of a large-amplitude
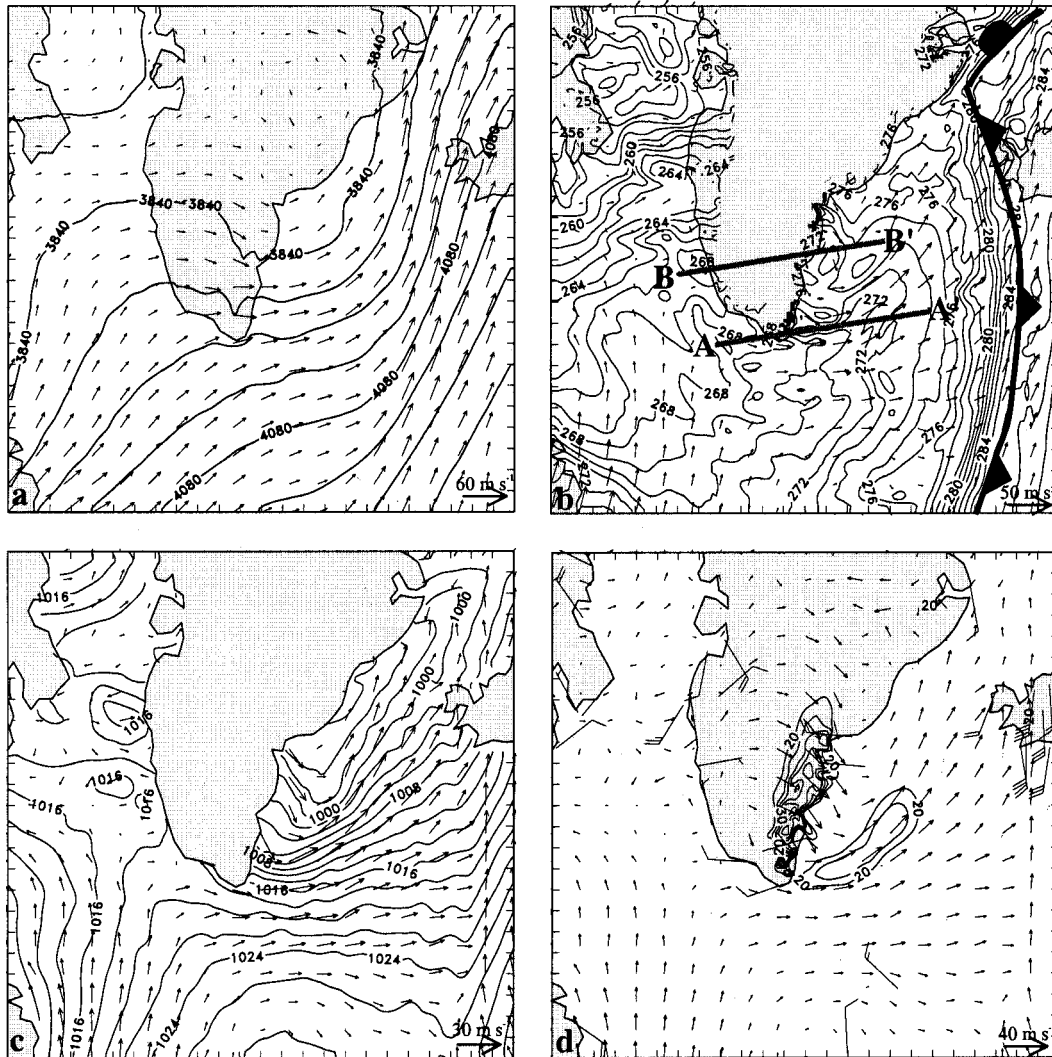

Fig. 8. The COAMPS simulated (a) 600-hPa geopotential height field (60 m contour interval) and wind vectors (every 8 grid points), (b) 1200-m potential temperature field (1 K isotherm interval) and wind vectors, (c) mean sea-level pressure field (2 hPa isobar interval) and 10-m wind vectors, and (d) 10-m wind speed greater than 20 m s^{-1} (2.5 m s^{-1} isotach interval) and wind vectors for 0600 UTC 29 January 1997 (18 h). Surface wind observations are shown in (d) (one full barb represents 5 m s^{-1}). The tick mark spacing on the boundary represents a distance of 90 km (3 grid intervals).

gravity wave is evident in the 600-hPa geopotential height field above the eastern south coast (Fig. 8a). The 1200-m (above sea level) potential temperature field (Fig. 8b) shows the north–south oriented polar cold front and associated baroclinicity located near the eastern end of the domain. The superimposed 1200-m wind vectors reveal that the upstream region is characterized by weak flow (<5 m s^{-1}), whereas the downstream lee contains strong flow in excess of 20 m s^{-1}. The mean sea-level pressure field (Fig. 8c) shows the weak pressure gradient at the western side of the Greenland tip and strong pressure gradient (20 hPa in 400 km) to the east. The 10-m wind velocity (Fig. 8d) flows anticyclonically over the top of Greenland and accelerates to greater 30 m s^{-1} upon descent of the eastern lee. The weak low-level flow upstream of southern Greenland extends nearly to the western boundary of the nested grid. A well-defined elliptical wind maximum greater than 25 m s^{-1} extends downstream toward the east from the southern tip. The wind speed minimum within the lee trough, poleward of the tip jet, results from flow splitting and dissipation processes associated with low-level wave breaking and is characterized by a Bernouli deficit. Conversely, the flow associated with the tip jet

remains laminar, does not undergo turbulent breaking and approximately conserves Bernouli function. The upstream flow contains positive vertical shear ($\partial V/\partial z > 0$) as can be seen from the 30-m s^{-1} difference between the 600-hPa and 10-m cross-Greenland winds (Figs. 8a, d, respectively), which is in first-order geostrophic thermal balance with the upstream north–south baroclinicity (Fig. 8b), consistent with colder air to the north. It is noteworthy that the sparse surface wind observations are in general agreement with the model simulated low-level winds (Fig. 8d).

Fig. 9 illustrates the 1200-m flow characteristics just below the mid-altitude of the maximum terrain elevation, which coincides with the level of maximum wind speed in the Greenland tip jet. The wind velocity field (Fig. 9a) shows: (i) the weak low-level flow upstream from Greenland, which extends upward from the surface (Fig. 8d) to the 1200-m level, and (ii) the tip jet (maximum >30 m s^{-1}) in the lee extending over $3L$ (600 km) downstream. The 1200-m PV distribution contains a filament (>0.5 PVUs) that extends $\sim L$ (300 km) downstream from the tip (Fig. 8b) and emanates from a region of low-level wave breaking.

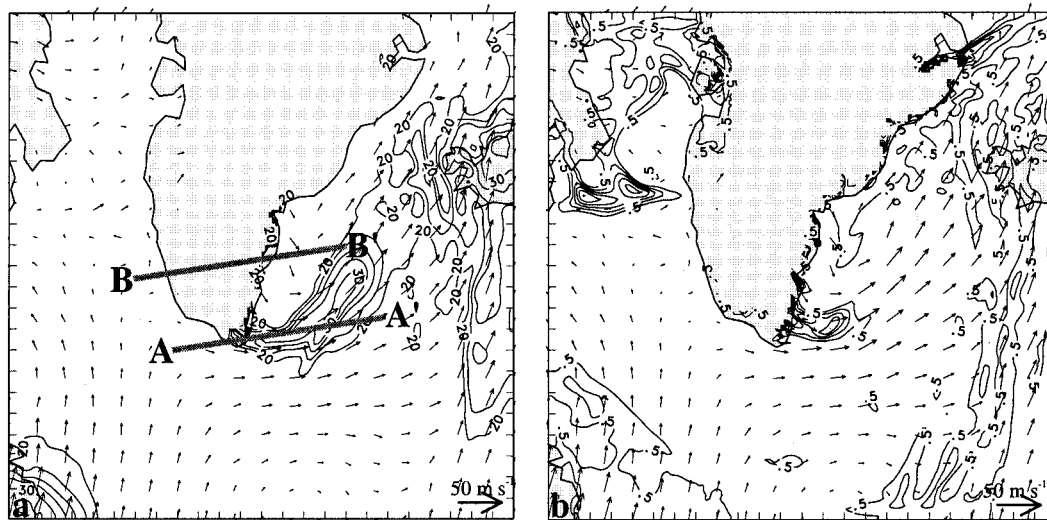Fig. 10 presents two vertical cross sections along the flow over Greenland that illustrate the differ-

Fig. 9. The COAMPS simulated (a) 1200-m wind speed greater than 20 m s^{-1} (2.5 m s^{-1} isotach interval) and wind vectors (every 8 grid points), and (b) 1200-m PV field (0.5 pvu contour interval) for 0600 UTC 29 January 1997 (18 h). PV values less than 0.5 pvu are suppressed in (b). The tick mark spacing on the boundary represents a distance of 90 km (3 grid intervals).
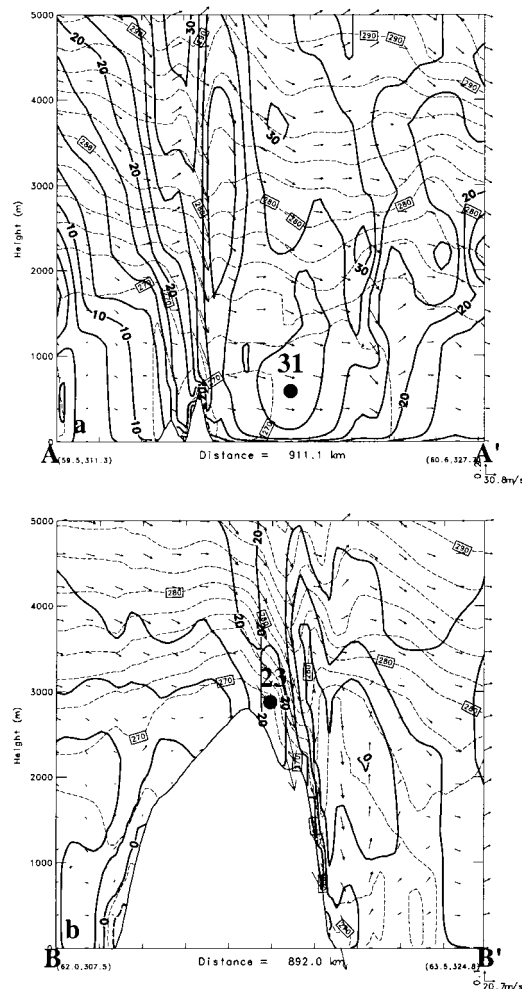
Fig. 10. Vertical cross section of potential temperature (dashed) and section-parallel wind speed (solid) and vectors taken along line (a) AA′ and (b) BB′ of Figs. 8b, 9a for 0600 UTC 29 January 1997 (18 h). The isotherm interval is 2 K and the isotach interval is 5 m s^{-1}. The tick mark spacing on the abscissa represents a distance of 90 km (3 grid intervals).

ence in vertical structure between the air flow over the broad and high southern portion of Greenland, in contrast with air flow over the significantly narrower and smaller southern tip. The cross-section analysis of potential temperature and section-parallel wind speed (Fig. 10a) taken along the projection line AA′ of Figs. 8b and 9a, shows: (i) the deep layer of upstream vertical wind shear, (ii) the relatively laminar flow over the Greenland

tip, (iii) the downstream core of the ~30 m s^{-1} tip jet located near 1200 m, (iv) a surface-based super-adiabatic layer downstream from the tip arising from the colder air flowing from the ice sheet and low lands overlying the relatively warmer sea, and (v) the vertical growth of the marine boundary layer downstream, with the wind speed maximum positioned near the top of the mixed layer. The companion cross section (Fig. 10b) to the north of Fig. 10a constructed along line BB′ passes through the region of extreme low-level wave breaking in the lee and shows weak low-level flow due to splitting and turbulent dissipation of momentum in the lee. The wind-speed gradient between the core of the tip jet and weak winds to the north in the wake is linked to the meridional differential in the intensity of wave breaking (Schär and Smith, 1993; Smith et al., 1997) along with a corresponding differential response in momentum dissipation and Bernouli function. The tip jet is in qualitative geostrophic thermal balance with the thermal gradient in the mixed-layer (Fig. 8b). A differential heat flux gradient exists between the laminar flow near the tip of Greenland and the turbulent wave breaking to the north. Understandably, near the surface this thermal-wind balance is not maintained.

Unfortunately, there are few in situ observations with which to evaluate the representativeness of the mesoscale simulated flows in this remote region. The NASA Scatterometer (NSCAT) on board the ADEOS polar orbiting satellite provided indirect verification of the general wind flow and embedded tip jet in the Greenland lee for this situation (Fig. 11). The NSCAT instrument has a resolution of ~25 km with characteristic RMSE of ~2–4 m s^{-1}. The model simulated low-level winds and tip jet (Fig. 8d) are in general agreement with the surface wind estimates.

5.2. The 18 February 1997 Greenland tip jet

The second simulation of orographically enhanced flow in the lee of the southern tip of Greenland, is taken from FASTEX IOP 17, during 17–18 February 1997. A 24-h simulation was initialized with observations at 1200 UTC 17 February and verified at 1200 UTC 18 February 1997 (Fig. 12). The 400-hPa geopotential height and wind velocity field (Fig. 12a) shows a large-scale (3000-km) arctic trough on the polar vortex
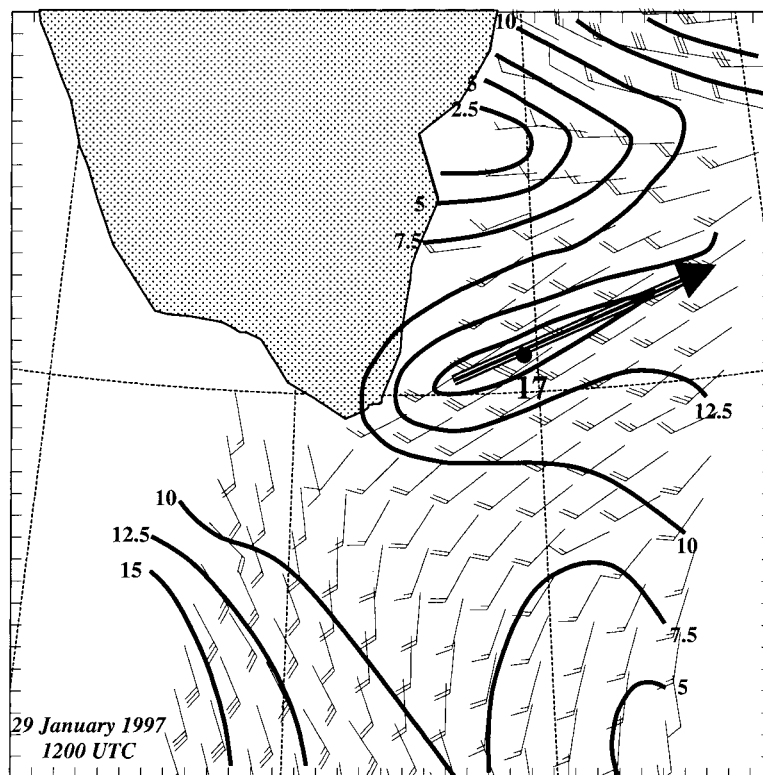
Fig. 11. Near-surface wind speed analysis (2.5 m s^{-1} isotach interval) based on observations (wind barbs) from NSCAT winds for 1200 UTC 29 January 1997.

and associated east–west oriented trough axis across the southern tip of Greenland. Note, there is little or no flow upstream or over the tip. The 1500-m simulated potential temperature (Fig. 12b) shows cold-air streaming southeastward upstream from the ice-covered Labrador Sea toward the south tip of Greenland. The feature of interest is the ~ 10 K thermal gradient across 100 km in the lee of the Greenland tip within the tip-jet front. The superimposed 1500-m wind vectors show the 10 m s^{-1} wind flow upstream from the Labrador Sea increasing to >40 m s^{-1} downstream, where the cold plume extends beyond the lee of Greenland at the southern edge of the front. The sense of differential thermal advection across the front is noteworthy, where strong cold-air advection to the south of the tip-jet front constitutes: (i) the geostrophic component of thermal frontogenesis, and (ii) the thermally-indirect source term for the Sawyer (1956)–Eliassen (1962) circulation

equation, (i.e., cyclonically-sheared differential cold-air advection). The mean sea-level pressure (Fig. 12c) shows a weak gradient at the western side of the Greenland tip and strong gradient (40 hPa in 300 km) to the east. In contrast to the previous case (Fig. 8d), there is no discernable westerly component of the surface flow (Fig. 12d) over the high terrain. It is noteworthy that easterly flow >20 m s^{-1} exists over the northern glacial cap. The 10-m northwesterly flow from the Labrador Sea in the upstream of Greenland accelerates and rotates cyclonically westward into the >30 m s^{-1} tip jet in the eastern lee. The limited available surface observations are in close agreement with the simulated winds (Fig. 12d).

Fig. 13 illustrates the 1500-m flow characteristics below the mid-altitude of the maximum terrain elevation and near the tip-jet core. The wind velocity field (Fig. 13a) shows: (i) the weak low-level flow to the north of the tip jet, which
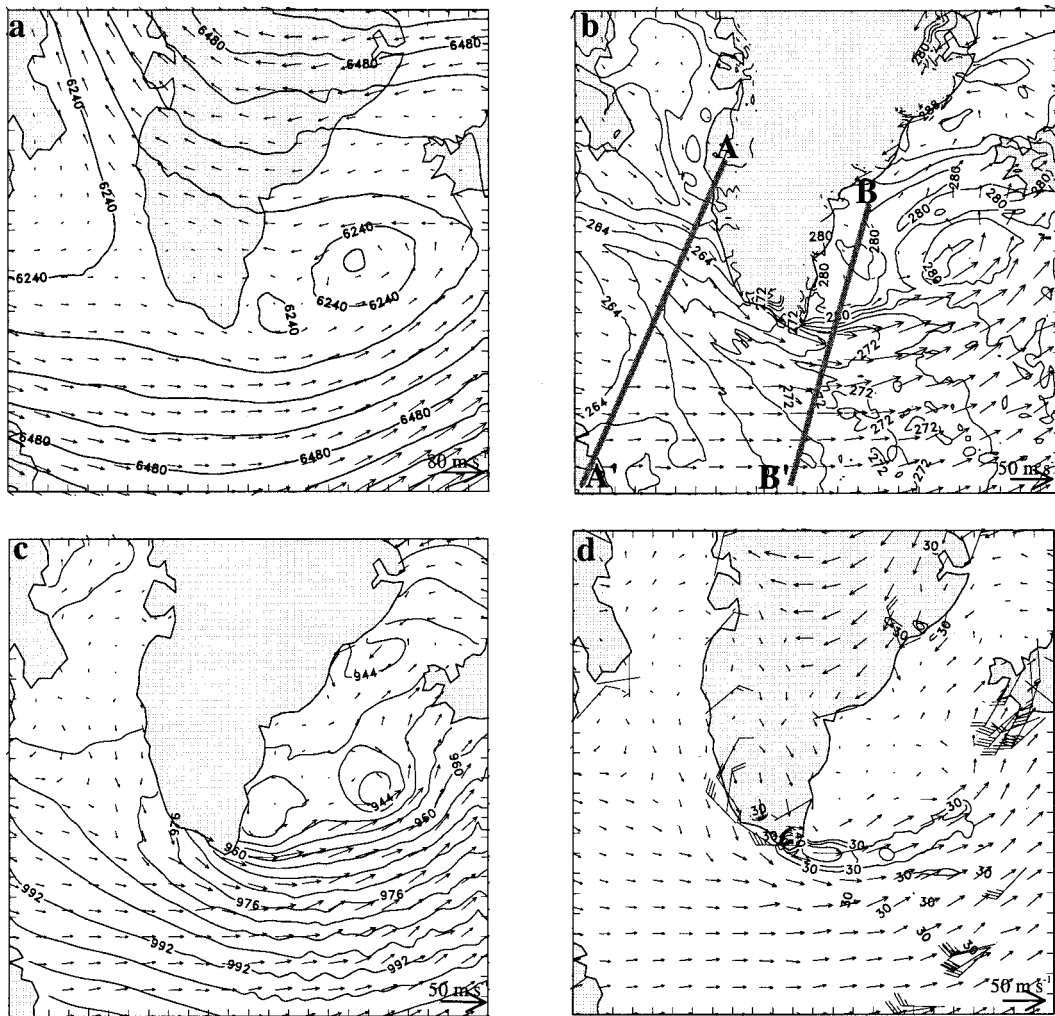
Fig. 12. The COAMPS simulated (a) 400-hPa geopotential height field (60 m contour interval) and wind vectors (every 8 grid points), (b) 1500-m potential temperature field (2 K isotherm interval) and wind vectors, (c) mean sea-level pressure field (4 hPa isobar interval) and 10-m wind vectors, and (d) 10-m wind speed greater than 30 m s^{-1} (2.5 m s^{-1} isotach interval) and wind vectors for 1200 UTC 18 February 1997 (24 h). Surface wind observations are shown in (d) (one full barb represents 5 m s^{-1}). The tick mark spacing on the boundary represents a distance of 90 km (3 grid intervals).

extends upward from the surface (Fig. 12d) to the 400-hPa level (Fig. 12a), and (ii) the tip jet (maximum >40 m s^{-1}) in the lee extending ~4L downstream. The 1500-m PV distribution (Fig. 13b) contains a filament (>0.5 PVUs) that extends downstream from the tip and emanates from a region of low-level wave breaking. The 1500-m PV maximum in the northern Labrador Sea is associated with vertical differential radiative cool-

ing within the arctic boundary layer above the sea ice, with the leading edge of the PV maximum at the ice edge.

Figs. 14a, b presents vertical cross sections approximately normal to the flow taken upstream (west) and downstream (east) of the Greenland tip jet, respectively and illustrate the vertical structure of potential temperature and section normal wind for 1200 UTC 18 February (after 24-h of simula-
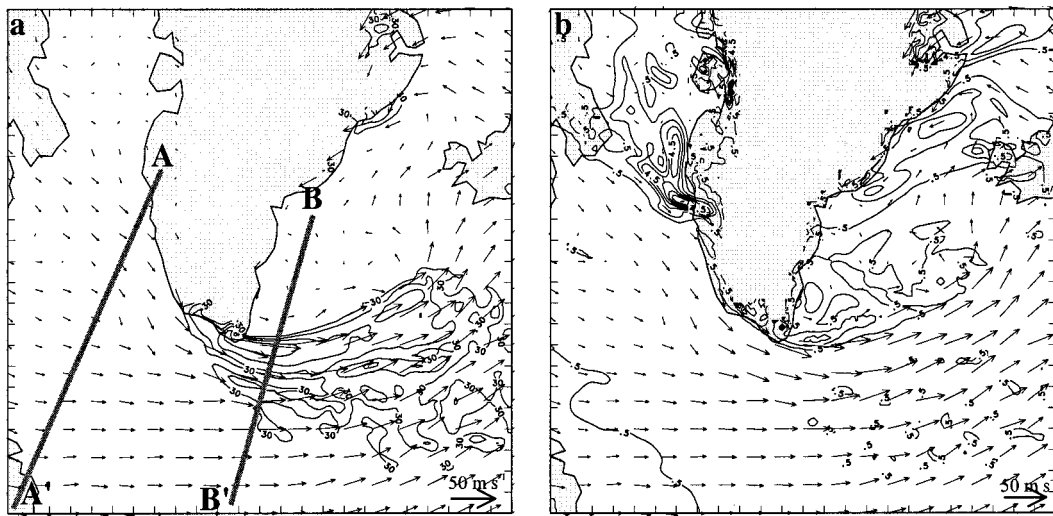
Fig. 13. The COAMPS simulated (a) 1500-m wind speed greater than 30 m s^{-1} (5.0 m s^{-1} isotach interval) and wind vectors (every 8 grid points), and (b) 1500-m PV field (1.0 pvu contour interval) for 1200 UTC 18 February 1997 (24 h). PV values less than 0.5 pvu are suppressed in (b). The tick mark spacing on the boundary represents a distance of 90 km (3 grid intervals).
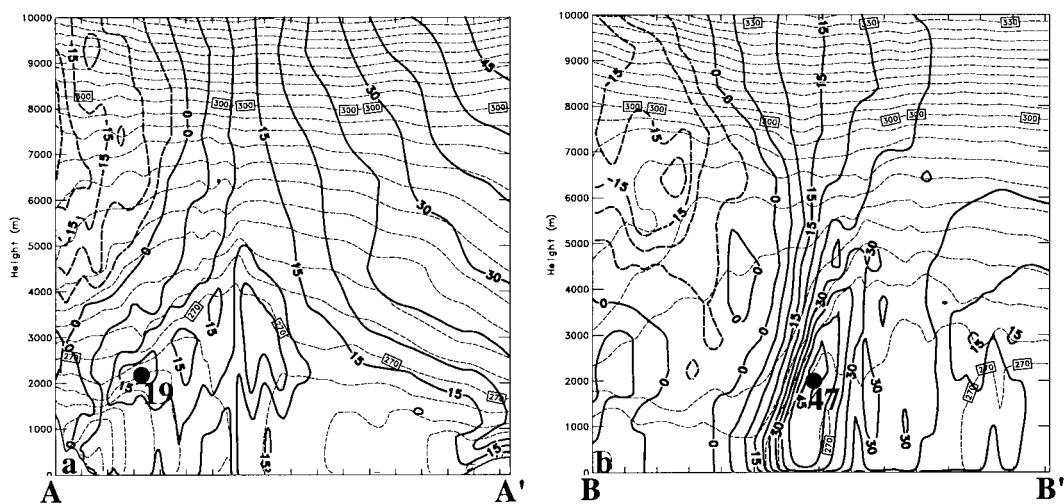

Fig. 14. Vertical cross section of potential temperature (dashed) and section-normal wind speed (solid) taken along line (a) AA′ and (b) BB′ of Figs. 12b and 13a for 1200 UTC 18 February 1997 (24 h). The isotherm interval is 3 K and the isotach interval is 5 m s^{-1}. The tick mark spacing on the abscissa represents a distance of 90 km (3 grid intervals).

tion). The upstream section (Fig. 14a) taken across the Labrador Sea along line AA′ of Figs. 12b and 13a shows: (i) the shallow arctic boundary layer and capping inversion to the north and growth of the mixed layer to a maximum height of 4000 m in the middle of the sea, (ii) the ∼20 m s^{-1} northwesterly wind maximum that characterize the air parcels that subsequently enter the 45 m s^{-1} tip jet to the east, and (iii) the reverse wind shear southeasterlies aloft. The sloping boundary layer

inversion along the east coast of Greenland arises from the integrated effects of differential heat fluxes, with a diabatic heating minimum near the coast and maximum in the middle of the Labrador Sea, similar to the Spitzbergen ice-edge jet and front documented by Shapiro et al. (1987). The downstream cross section (Fig. 14b) taken through the core of the low-level tip jet along line BB′ of Figs. 12b and 13a shows: (i) the $\sim 45\ \mathrm{m\ s^{-1}}$ core of the tip jet at 2 km, (ii) substantial vertical shear above the jet center, (iii) the southward sloping with height baroclinic zone associated with the tip jet front that is in qualitative geostrophic thermal balance with the jet, and (iv) the $\sim 20\ \mathrm{m\ s^{-1}}$ easterly upper-level (~ 6.5 km) jet stream over the north portion of Greenland.

As in the former case, only limited direct observations were available to verify the flows described above. Fig. 15 presents a NOAA polar-orbiting satellite infrared image valid at 1428 UTC 18 February. The key features include: (i) cloud streets emanating from the Labrador Sea oriented parallel to the cold-air outflow, which transform into cellular convection in the downstream destabilized boundary layer, (ii) the progressively increasing cloud-top heights evinced by the decreasing cloud-top temperatures of the flow around the tip, and (iii) the abrupt discontinuity in cloud structure. The shallow stratiform clouds to the north of the tip jet are in agreement with the simulated moisture discontinuity across the tip jet-front system (not shown). These salient cloud features associated with the Greenland tip
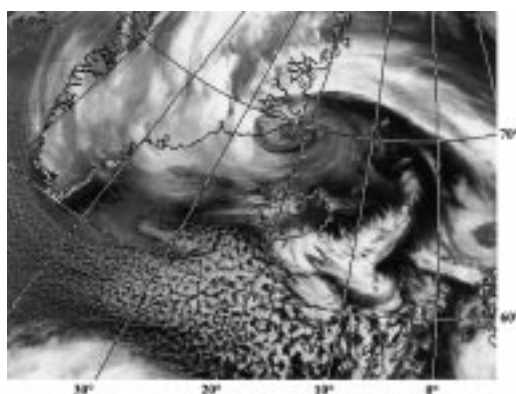

Fig. 15. NOAA polar-orbiting satellite infrared image valid at 1428 UTC 18 February.

jet are quite similar to those described by Scorer (1988).

Fig. 16 presents the surface wind speeds at 1400 UTC 18 February 1987 derived from Special Sensor Microwave/Imager (SSM/I) with an effective resolution of 25 km and RMSE of $\sim 5\ \mathrm{m\ s^{-1}}$. The SSM/I winds show the jet emanating from the tip of Greenland and extending eastward ~ 1000 km with maximum wind speed of 35 m s^{-1}, remarkably consistent with the simulated near-surface winds (Fig. 12d).

6. Summary

6.1. Discussion

A frequent issue that arises is the relevance of idealized theories and their simulations to atmospheric flows past complex topography found in nature. The idealizations are simplifications of reality based on smooth topography derived from algebraic functions, barotropic and temporally invarient basic states, and simplifying approximations to the full set of equations applied through analytical solution and numerical integration. In contrast, complex numerical simulations using full-terrain resolving models containing sophisticated physical parameterizations, though capable of replicating realistic flows, do not provide a clear theoretical and physical understanding of the phenomena. One step toward relaxing one of these simplifying constraints is the incorporation of realistic topography into the idealized simulations (Section 4). Fig. 17 shows a simulation using the actual Greenland topography performed with identical idealized parameters as in Fig. 3a. The results illustrate the robust nature of flow response, such as the upstream northward deflection, wake and associated eddies, and the tip jet. However, the impact of the non-Gaussian orography results in significant differences in the flows, particularly in the dissipative zone, the along-flow extent of the tip-jet downstream and eastern lee where the fjords contribute to complex outflows. The non-Gaussian character of the Greenland escarpment is greatest in the southeast and northwest, where the flows differ considerably from one another.

Of the two real-data topographic flow simulations described above, the flow during IOP 8 (Subsection 5.1) most resembles the idealized f-plane experiments (Fig. 3a). The similarities
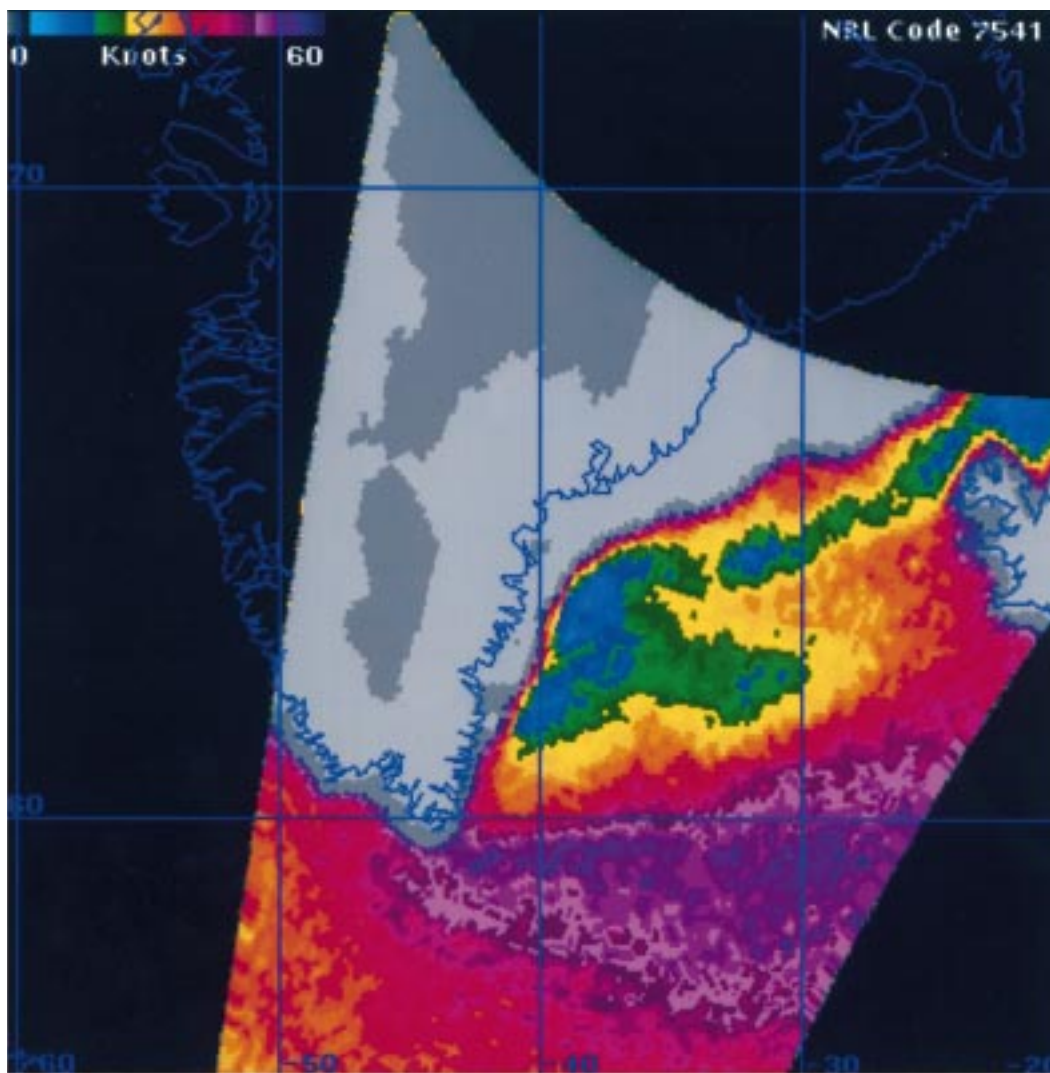
Fig. 16. Near-surface wind speed derived from SSM/I for 1400 UTC 18 February 1997.

between IOP 8 and the idealized simulation include: (i) the tip jet, (ii) flow deflection along the upstream slope, (iii) downslope warming maximized in the lee to the north of the jet, and (iv) reverse-shear baroclinicity at the tip. The upstream westerly flow at the surface in IOP 8 is weak ($5\,\mathrm{m\,s^{-1}}$) and increases with height to $30\,\mathrm{m\,s^{-1}}$ at 5 km. It is noteworthy that the effect of this forward vertical shear (westerlies increasing with height) associated with upstream baroclinicity is not included in previous idealized experi-

ments and may lead to a more complex lee-side response that has not been completely addressed for three-dimensional topographic flows. In both the idealized and real-data (IOP 8) simulations, the cross-mountain winds near obstacle peak are similar, however the thermal stratification in IOP 8 was substantially weaker, and therefore $\hat{h}$ smaller than the idealized experiments. It follows from the idealized experiments (Fig. 7) that one should expect a weaker tip jet response with a reduction in upstream $\hat{h}$, especially in the presence of surface
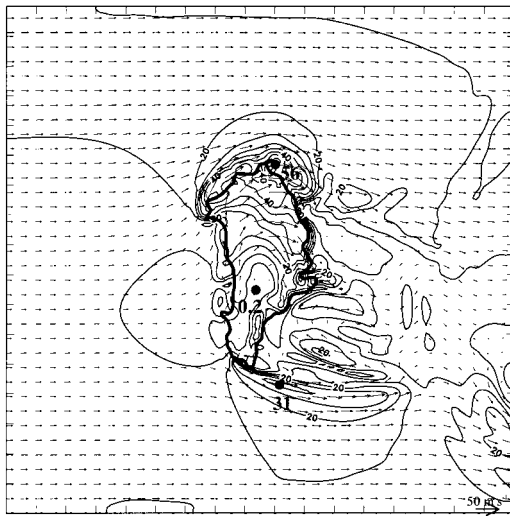
Fig. 17. The lowest model-level (10 m) winds (vectors every 5 grid points) for a simulation on an *f*-plane for realistic Greenland topography (96 h). The isotach interval is 2.5 m s^{-1}. The tick mark spacing on the boundary represents a distance of 300 km (10 grid intervals). The 750-m terrain contour ($h/4$) is shown by the bold contour.

fluxes. However, the IOP-8 35 m s^{-1} tip jet is stronger than predicted from idealized theory, underscoring the possible importance of the baroclinic character (forward shear) of the upstream wind profile. In addition, the vertical differential in horizontal advection (warm-air advection in the southwesterly flow aloft, not shown) upstream of the southern portion of Greenland may act to increase the low-level blocking (Garner, 1999) and therefore the tip jet (Fig. 7). The downslope warming is amplified in both the IOP 8 and the Gaussian topography experiments due to wave breaking and near-surface turbulent mixing in the lee, leading to a baroclinic enhancement of the tip jet. Furthermore, katabatic flow common to the Greenland slopes may also be an important factor in these flow regimes. However, the overall qualitative salient characteristics of the tip jet are structurally similar in the IOP-8 and idealized experiments.

The fundamental characteristics of IOP 17 (Subsection 5.2) differ substantially from that of the idealized and IOP 8 simulations. In contrast to IOP 8, the basic flow upstream of the southern tip for IOP 17 contains very weak low-level cross-obstacle winds (<5 m s^{-1}) with small vertical

shear and stronger stability below mountain top. A critical level is present with easterly flow throughout the troposphere over the northern portion of Greenland, in contrast to the deep westerlies of the previous situation. A key feature of IOP 17 is the southeastward transport of cold-air from the Labrador Sea trapped beneath the critical level, which culminates in the extreme differential cold-air advection (viz., horizontal shear frontogenesis) at the tip and lee of Greenland (Fig. 12b). The cold plume passes south of the tip and downstream to the east. Concurrent with the tip jet development is the frontogenesis associated with horizontal deformation in the lee. This arises through the juxtaposition of low-level cold-air advection from the Labrador Sea south of the tip with the warming through adiabatic descent to the north. In contrast, the idealized and IOP 8 situation of tip-jet frontogenesis is dominated by the tilting effect through differential subsidence.

Bernouli function diagnostics are widely used to diagnose Lagrangian energetics of orographic flows (Schär and Smith, 1993; Schär and Durran, 1997; Pan and Smith, 1999). For the idealized case discussed in Section 4, parcels escaped Bernouli loss accelerating down the pressure gradient into the tip jet. In contrast, the weak speed wake situated immediately to the north of the tip jet is characterized by a Bernouli deficit. Similar Bernouli behaviour is contained within the simulated observed flows, in spite of the complexities of non-conservative processes at the lower boundary (e.g., friction, surface energy fluxes). However, quantitative diagnosis of the Bernouli budget is difficult in the presence of viscous, baroclinic, time-variant flow regimes associated with the selected cases.

A response of the enhanced near-surface wind speed associated with the tip jet, is the dramatic increase in the air–sea energy exchange processes. As an example, the model simulated surface-heat flux field for IOP 17 valid at 1200 UTC 18 February (Fig. 18) shows a region of upward surface heat flux >500 W m^{-2} extending >800 km downstream (eastward) from the Greenland tip, with the flux maximum oriented along the tip-jet axis. Additionally, the strong horizontal shear along the north and south sides of the tip jet is synonymous with regions of maximum and minimum $\nabla \times \tau_s$ (curl of the surface stress, τ_s) that may represent an important com-
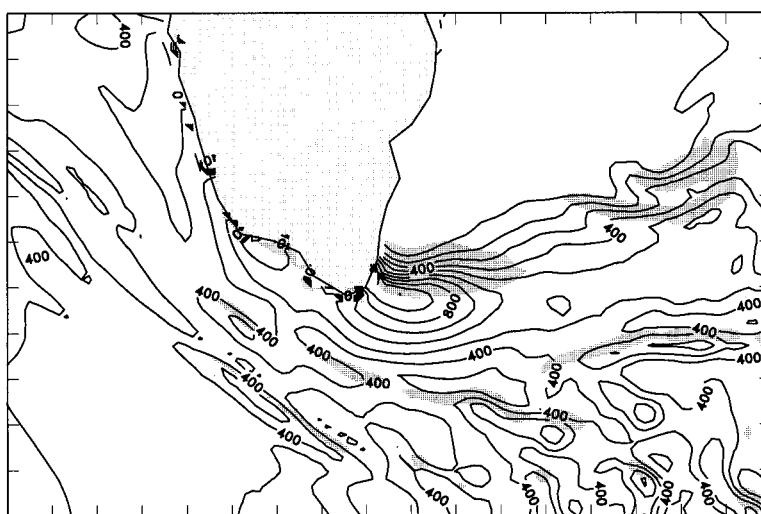
Fig. 18. Surface sensible heat flux (100 W m^{-2} contour interval) for 1200 UTC 18 February 1998. Values of $\nabla \times \tau_s$ greater than 2.0×10^{-5} N m^{-3} are shaded.

ponent of the regional oceanic circulation due to localized oceanic upwelling and downwelling (Fig 18). We would expect the Greenland tip jet to modulate the oceanic thermal-haline circulation because of large surface fluxes (Fig. 18), potentially long-duration of high winds (in the IOP 17 case, greater than 24 h), and frequent episodes of tip-jet occurrence.

6.2. Future directions

The above idealized and real-data simulations of complex orographic flows in the vicinity of Greenland highlight several unresolved issues and directions for future research. The numerical simulations of Buzzi et al. (1997), which indicate plumes of vorticity generated in the lee of Cape Adare, Antarctica, are suggestive that tip jet phenomena may be not be confined to Greenland. Observational documentation of flow response to synoptic-scale topographic obstacles is needed to determine whether tip jets may occur in other environments and geographical areas. With regard to idealized simulation research, one should consider more realistic orography and the effects of non-conservative boundary-layer and moist processes. Of particular importance is the relaxation of the barotropic constraint so as to include baroclinicity of the mean flow, both in the along- and cross-flow directions. In nature, the arctic

orographic flows of the type described above are sensitive to space/time variations ranging from anomalies in the arctic planetary-scale circulation to transient mesoscale disturbances. Therefore, further numerical studies should be undertaken to advance our understanding of high-latitude orographic flows. However, incessant numerical simulations performed in the absence of observational verification on the proper time and space scales can only lead to hypotheses of possible atmospheric responses. Observations from promising new space-based remote-sensing technologies such as polar-orbiting satellite sea-surface winds measured with passive and active microwave remote sensors and boundary-layer cloud drift winds tracked via geostationary satellites will yield limited, but valuable, validation of surface and boundary-layer flows almost exclusively over the sea. Further significant advancements in the understanding and prediction of orographic flows require the simultaneous use of the emerging-generation of numerical models in concert with airborne and surface-based in situ and remote observing systems from field campaigns. Finally, the future research should also consider the upscale impact of these orographically-induced jets on the synoptic-, planetary-, and climate-scale atmospheric and oceanic circulations as well as regional climate impacts.

7. Acknowledgements

REFERENCES

Buzzi, A, R. Cadelli and P. Malguzzi, 1997. Low-level jet simulation over the Southern Ocean in Antarctica. *Tellus* **49A**, 263–276.

Davis, C. 1997. The modification of baroclinic waves by the Rocky Mountains. *J. Atmos. Sci.* **54**, 848–868.

Davies, H. C. 1976. A lateral boundary formulation for multi-level prediction models. *Quart. J. Roy. Meteor. Soc.* **102**, 405–418.

Doyle, J. D., M. A. Shapiro, D. Bartels and R. Gall, 1998. The numerical simulation and validation of a breaking gravity wave during FASTEX. *16th Conference on weather analysis and forecasting*, Phoenix, AZ, Conference Proceedings, Amer. Meteor. Soc., 460–462.

Durran, D. R. and J. B. Klemp, 1983. A compressible model for the simulation of moist mountain waves. *Mon. Wea. Rev.* **111**, 2341–2361.

Eliassen, A. 1962. On the vertical circulation in frontal zones. *Geofys. Publ.* **24**, 147–160.

Eliassen, A. 1980. Balanced motion of a stratified, rotating fluid induced by bottom topograpy. *Tellus* **32**, 537–547.

Gal-Chen, T. and R. C. J. Somerville, 1975. On the use of a coordinate transformation for the solution of the Navier–Stokes equations. *J. Comput. Phys.* **17**, 209–228.

Garner, S. T. 1999. Blocking and frontogenesis by two-dimensional terrain in baroclinic flow. Part II: Analysis of flow stagnation mechanisms. *J. Atmos. Sci.* **56**, 1509–1523.

Gill, A. E. 1982. *Atmosphere–ocean dynamics*. Academic Press, New York.

Harshvardhan, R. Davies, D. Randall and T. Corsetti, 1987. A fast radiation parameterization for atmospheric circulation models. *J. Geophys. Res.* **92**, 1009–1015.

Hess, S. L. and H. Wagner, 1948. Atmospheric waves in the northwestern United States. *J. Meteor.* **5**, 1–19.

Hodur, R. M. 1997. The Naval Research Laboratory's Coupled ocean/atmosphere mesoscale prediction system (COAMPS). *Mon. Wea. Rev.* **125**, 1414–1430.

Hogan, T. F. and T. E. Rosmond, 1991. The description of the U.S. Navy Operational Global Atmospheric Prediction System's spectral forecast model. *Mon. Wea. Rev.* **119**, 1786–1815.

Huppert, H. E. and J. W. Miles, 1969. Lee waves in a stratified flow. Part 3: Semi-elliptical obstacles. *J. Fluid Mech.* **35**, 481–496.

Joly, A. et al. 1997. The fronts and atlantic storm-track experiment (FASTEX): Scientific objectives and experimental design. *Bull. Amer. Meteor. Soc.* **78**, 1917–1940.

Kain, J. S. and J. M. Fritsch 1993. Convective parameterization for mesoscale models: The Kain–Fritsch scheme. The representation of cumulus convection in numerical models, *Meteor. Monogr.* **46**, Amer. Meteor. Soc., pp. 165–170.

Klemp, J. and R. Wilhelmson, 1978. The simulation of three-dimensional convective storm dynamics. *J. Atmos. Sci.* **35**, 1070–1096.

Louis, J. F. 1979. A parametric model of vertical eddy fluxes in the atmosphere. *Bound.-Layer Meteor.* **17**, 187–202.

Lynch, P. and X.-Y. Huang, 1992. Initialization of the HIRLAM model using a digital filter. *Mon. Wea. Rev.* **120**, 1019–1034.

Ólafsson, H. and P. Bougeault, 1996. Nonlinear flow past an elliptical ridge. *J. Atmos. Sci.* **53**, 2465–2489.

Ólafsson, H. and P. Bougeault, 1997. The effect of rotation and surface friction on orographic drag. *J. Atmos. Sci.* **54**, 193–210.

Orlanski, I. 1976. A simple boundary condition for unbounded hyperbolic flows. *J. Comput. Phys.* **21**, 251–269.

Pan, F. and R. B. Smith, 1999. Gap winds and wakes. SAR observations and numerical simulations. *J. Atmos. Sci.* **56**, 905–923.

Peng, M. S., S.-W. Li, S. W. Chang and R. T. Williams,

1995. Flow over mountains: Coriolis force, transient troughs and three dimensionality. *Quart. J. Roy. Meteor. Soc.* **121**, 593–613.

Pierrehumbert, R. T. 1984. Linear results on the barrier effects of mesoscale mountains. *J. Atmos. Sci.* **41**, 1356–1367.

Pierrehumbert, R. T. 1985. A theoretical model of orographically modified cyclogenesis. *J. Atmos. Sci.* **42**, 1244–1258.

Pierrehumbert, R. T. and B. Wyman, 1985. Upstream effects of mesoscale mountains. *J. Atmos. Sci.* **42**, 977–1003.

Queney, P. 1948. The problem of air flow over mountains: A summary of theoretical studies. *Bull. Amer. Meteor. Soc.* **29**, 16–26.

Rutledge, S. A. and P. V. Hobbs, 1983. The mesoscale and microscale structure of organization of clouds and precipitation in midlatitude cyclones. VIII: A model for the "seeder-feeder" process in warm-frontal rainbands. *J. Atmos. Sci.* **40**, 1185–1206.

Sawyer, J. S. 1956. The vertical circulation at meteorological fronts and its relation to frontogenesis. *Proc. Roy. Soc. London* **A234**, 346–362.

Scorer, R. S. 1988. Sunny Greenland. *Quart. J. Roy. Meteor. Soc.* **114**, 3–29.

Schär, C. 1993. A generalization of Bernouli's theorem. *J. Atmos. Sci.* **50**, 1437–1443.

Schär, C. and D. R. Durran 1997. Vortex formation and vortex shedding in continuously stratified flows past isolated topography. *J. Atmos. Sci.* **54**, 534–554.

Schär, C. and R. B. Smith, 1993. Shallow-water flow past isolated topography. Part I: Vorticity production and wake formation. *J. Atmos. Sci.* **50**, 1373–1400.

Schutts, G. 1998. Idealized models of the pressure drag force on mesoscale mountain ridges. *Contrib. Amos. Phys.* **71**, 303–313.

Shapiro, M. A., L. S. Fedor and T. Hampel, 1987. Research aircraft measurments of a polar low over the Norwegian Sea. *Tellus* **39A**, 272–306.

Smith, R. B. 1979. The influence of mountains on the atmosphere. *Advances in Geophysics* **21**, Academic Press, New York, 87–230.

Smith, R. B. 1980. Linear theory of stratified hydrostatic flow past an isolated mountain. *Tellus* **32**, 348–364.

Smith, R. B. 1982. Synoptic observations and theory of orographically disturbed wind and pressure. *J. Atmos. Sci.* **39**, 60–70.

Smith, R. B. 1986. Further development of a theory of lee cyclogenesis. *J. Atmos. Sci.* **41**, 1582–1602.

Smith, R. B. 1989. Hydrostatic flow over mountains. *Advances in Geophysics* **31**, Academic Press, New York, pp. 1–41.

Smith, R. B. and S. Grønás, 1993. Stagnation points and bifurcation in 3-D mountain airflow. *Tellus* **45A**, 28–43.

Smith, R. B., A. C. Gleason, P. A. Gluhosky and V. Grubisic, 1997. The wake of St. Vincent. *J. Atmos. Sci.* **54**, 606–623.

Smolarkiewicz, P. K. and R. Rotunno, 1989. Low Froude number flow past three-dimensional obstacles. Part I: Baroclinically generated vortices. *J. Atmos. Sci.* **46**, 1154–1164.

Snyder, W. H., R. E. Thompson, R. E. Eskridge, I. P. Lawson, J. T. Castro, J. T. Lee, J. C. R. Hunt and Y. Ogawa, 1985. The structure of strongly stratified flow over hills: Dividing streamline concept. *J. Fluid Mech.* **152**, 249–288.

Thorsteinsson, S. 1988. Finite amplitude stratified flow past isolated mountains on an *f*-plane. *Tellus* **40A**, 220–236.

Thorsteinsson, S. and S. Sigurdsson, 1996. Orogenic blocking and deflection of stratified air flow on an *f*-plane. *Tellus* **48A**, 572–583.

Tibaldi, S., A. Buzzi and A. Speranza, 1990. Orographic cyclogenesis. *Extratropical cyclones*, C. Newton and E. O. Holopainen, Eds. Amer. Meteor. Soc., pp. 107–128.

Trüb, J. and H. C. Davies, 1995. Flow over a mesoscale ridge. pathways to regime transition. *Tellus* **47A**, 502–524.